Supporting Information

Engineering Active Site Reconstruction of Metal Hydroxide/Metal Molybdate Heterogeneous Interface Enhances the Electrochemical Water Oxidation Process

Xuanyu Zhou, [a] Junjun Zhang,[*, a] Mengyuan Zhang,[a,b] Xiaoqian Du,[a] Weiwei Bao,[c] Jie Han,[c,*] Xiu Lin[d], Pengfei Zhang*[,a,b], Zhenghong Luo [a,b]

[a]State Key Laboratory of High-Efficiency Utilization of Coal and Green Chemical Engineering. College of Chemistry and Chemical Engineering, Ningxia University, Yinchuan, Ningxia, 750021, China. Email: zhangjj089@nxu.edu.cn (J.J. Zhang); pfzhang@nxu.edu.cn (P. F. Zhang)

[b]School of Chemistry and Chemical Engineering, Shanghai Jiao Tong University, Shanghai, 200240, P. R. China Email: chemistryzpf@sjtu.edu.cn (P. F. Zhang)

[c]School of Materials Science and Engineering, Shaanxi University of Technology, Hanzhong 723000, Shaanxi, China. Email: hanjie@snut.edu.cn (J. Han)

[d]School of Materials Science and Engineering, Nanyang Technological University, 639798, Singapore.

List of Contents

1. Experimental section

1.1 Chemicals

$FeCl_3$ (A.R grade, Shanghai Aladdin Biochemical Technology Co., Ltd.), $(NH_4)_6Mo_7O_{24}$ (A.R grade, damas-beta®), $NiCl_2{\cdot}6H_2O$ (A.R grade, Shanghai Aladdin Biochemical Technology Co., Ltd.), $C_6H_{12}N_4$ (A.R grade, Sinopharm Chemical Reagent Co., Ltd.), CH_3CH_2OH (A.R grade, Sinopharm Chemical Reagent Co., Ltd.), TM were used as the substrate and purchased from Shanghai Hesen Electric Co., Ltd., and deionized water were all prepared in the laboratory. All chemical reagents have not been further purified.

1.2 Pretreatment of Titanium Mesh (TM)

TM was cut into small rectangular pieces of 1 cm×4 cm. After ultrasonic cleaning with 3 M HCl for 30 min, they were washed with deionized water and anhydrous ethanol three times. Afterward, it is placed in a 60°C oven for complete drying, yielding in the desired TM.

1.3 Synthesis of $Fe_2(MoO_4)_3$@TM

880 mg of $FeCl_3$ and 250 mg of $(NH_4)_6Mo_7O_{24}$ were dissolved in 30 mL of deionized water. The solution was stirred vigorously to ensure complete mixing. Subsequently, the mixed solution, along with the pretreated TM (1 cm × 4 cm) was placed into a 50-mL stainless steel autoclave lined with PTEF. The autoclave was maintained at 120°C for 6 hours. After the autoclave had cooled down naturally, the prepared electrode was rinsed repeatedly with deionized water and ethanol, and then dried in an oven at 60 °C to obtain $Fe_2(MoO_4)_3$@TM electrode.

1.4 Synthesis of $Ni(OH)_2$@TM

60 mg of $NiCl_2{\cdot}6H_2O$ and 105 mg of $C_6H_{12}N_4$ were dissolved in a homogeneous solution consisting of 15 mL of ethanol and 10 mL of deionized water. The resulting solution was magnetically stirred for 30 min. The mixed solution, along with the pretreated TM (1 cm×4 cm) was placed into a 50-mL stainless steel autoclave lined with PTEF. The autoclave was maintained at 120°C for 4 h. After the reactor cooled down to room temperature, the sample was washed three times with deionized water and ethanol, and then dried at 60°C to obtain $Ni(OH)_2$@TM electrode.

1.5 Electrochemical measurement

Electrochemical performance was evaluated using a CHI 660E electrochemical workstation with a standard three-electrode system, comprising a Hg/HgO reference electrode, a graphite counter electrode, a homemade nickel foam working electrode, and a homemade 1 M KOH electrolyte. Linear sweep voltammetry (LSV) measurements were conducted at a scan rate of 5 mV s^{-1} within a potential range of 0-1.1 V vs. Hg/HgO. The potentials were calibrated to the reversible hydrogen electrode (RHE) using the formula $E_{RHE} = E_{Hg/HgO} + 0.098 + 0.059 \times pH$. The overpotential ($\eta$) was calculated as $\eta = E_{RHE} - 1.23V$, based on the theoretical water splitting potential of 1.23 V. Tafel slopes were derived from log(current) versus potential plots obtained by recording LSV potentials and corresponding currents. Electrochemical impedance spectroscopy (EIS) was employed to measure electrode resistance at 0.6 V (vs. Hg/HgO) over a frequency range of 10^{-1}-10^5 Hz. Double-layer capacitance (C_{dl}) was assessed via cyclic voltammetry (CV) at varying scan rates (10-100 mV/s) within the non-Faradaic potential region. Operando EIS measurements were performed to generate Nyquist and Bode plots, and stability tests including multi-step current, multi-step voltage, and long-term durability assessments were conducted.

1.6 Material characterizations

X-ray diffraction (XRD) patterns were recorded on a Rigaku MiniFlex 600-C X-ray diffractometer with Cu-Kα radiation at a scan rate of 5° min^{-1}. Electron paramagnetic resonance (EPR) spectra were collected on a Bruker A300 paramagnetic spectrometer at room temperature under vacuum. Raman measurements were performed using a Raman JY HR800 spectrometer in the wavenumber region of 150-600 cm^{-1}. Scanning electron microscopy (SEM) characterizations were conducted using a JSM-7800F microscope from JEOL. Transmission electron microscopy (TEM) and high-resolution transmission electron microscopy (HRTEM) measurements were taken with a JEOL JEM-F200 microscope. X-ray photoelectron spectroscopy (XPS) measurements were conducted on a Kratos Axis Ultra DLD spectrometer. In-situ Raman measurements were performed using a Raman JY HR800 coupled with an EC-Raman flow cell (Beijing Scistar Technology, China) in the wavenumber range of 200-1200 cm^{-1}. A 50× long working distance objective (8 mm) was used, and the excitation laser with a wavelength of 532 nm was generated from a He-Ne laser with a power of approximately 6 mW. Data acquisition involved Raman readings at various constant potentials (1.30-1.70 V vs. RHE) with a stabilization period of 20 seconds prior to each measurement. For Raman measurements, a carbon rod was used as the counter electrode, Hg/HgO as the reference electrode, and the electrolyte was 1.0 M KOH solution. In-situ attenuated total reflectance-Fourier transform infrared spectroscopy (ATR-FTIR) was performed using a BRUKER INVENIO R spectrometer to detect intermediate signals of the electrocatalysts during the oxygen evolution reaction (OER) within a potential range of 1.20-1.65 V vs RHE. The experiment was conducted with a potential interval of 0.05 V vs RHE. The catalyst was labeled through five cycles of cyclic voltammetry (CV) in 1M KOH, using $H_2{}^{18}O$ as the solvent. Subsequently, the obtained electrode was rinsed several times with $H_2{}^{16}O$ and dried in an oven to remove any residual $H_2{}^{18}O$. DEMS measurements were conducted in 1M KOH solution with an applied potential, using $H_2{}^{16}O$ as the solvent. Mass spectrometry was employed to conduct real-time measurements of gas with different molecular weights generated during the OER.

1.7 DFT calculation method

All calculations were conducted within the framework of the Density Functional Theory (DFT), utilizing the Projector Augmented Wave (PAW) method implemented in the Vienna Ab initio Simulation Package (VASP) [1]. The exchange-correlation potential was approximated using the Generalized Gradient Approximation (GGA) of Perdew, Burke, and Ernzerhof (PBE) [2]. The DFT-D3 method was employed to account for long-range van der Waals interactions [3]. To address the strong correlation of d-electrons in Ni and Fe elements, a Hubbard-U term was introduced, with values set to 6.2 and 5.3 for Ni and Fe, respectively. Spin polarization was taken into account in the calculations.

The NiOOH(110) surface consists of 24 Ni, 48 O, and 24 H atoms, while the FeOOH(110) surface comprises 24 Fe, 48 O, and 24 H atoms. For the NiOOH(110)/FeOOH(110) and FeOOH(110)/NiOOH(110) heterostructures, the composition includes 12 Ni, 12 Fe, 48 O, and 24 H atoms. A vacuum layer of 16 Å was added perpendicular to the slabs to mitigate artificial interactions between periodic images.

To ensure convergence of the total energy, a plane-wave basis set with a kinetic energy cutoff of 450 eV and the Monkhorst-Pack k-point sampling scheme [4] with a grid spacing of $2\pi\times0.04$ $Å^{-1}$ were employed. Convergence criteria for ionic and electronic optimizations were set to 0.02 eV/Å

and 1×10^{-5} eV, respectively. The adsorption energy (ΔE) of the M group (M = OH, O, OOH, O_2) on the substrate surface was defined as follows: $\Delta E = E_{*M} - (E_* + E_M)$, where *M and * represent the adsorbed M group on the substrate and the pure substrate, respectively, and EM denotes the energy of the isolated M group. Note that the original equation provided (ΔE = EM - (E + EM)) contains an error and has been corrected here.

The adsorption energies follow the method:

$\Delta E_{*O} = E(sub/O) - E(sub) - E(H_2O)-E(H_2)$

$\Delta E_{*OH} = E(sub/OH) - E(sub) - E(H_2O)-E(H_2)/2$

$\Delta E_{*OOH} = E(sub/OOH) - E(sub) - 2\times E(H_2O)- 3\times E(H_2)/2$

$\Delta E_{*O2} = E(sub/O_2) - E(sub) - E(O_2)$

Where E(sub/O), E(sub/OH) and E(sub/OOH) represent the total energies of O, OH, OOH , and O_2 groups on the substrate. E(sub), $E(H_2O)$, and $E(H_2)$ are the total energies of pure substrate, water, hydrogen gas, and oxygen gas respectively. The free energies were calculated by including the zero-point vibrational energy and entropy as implemented in the VASPKIT package[5].

2. Supplementary Figures:

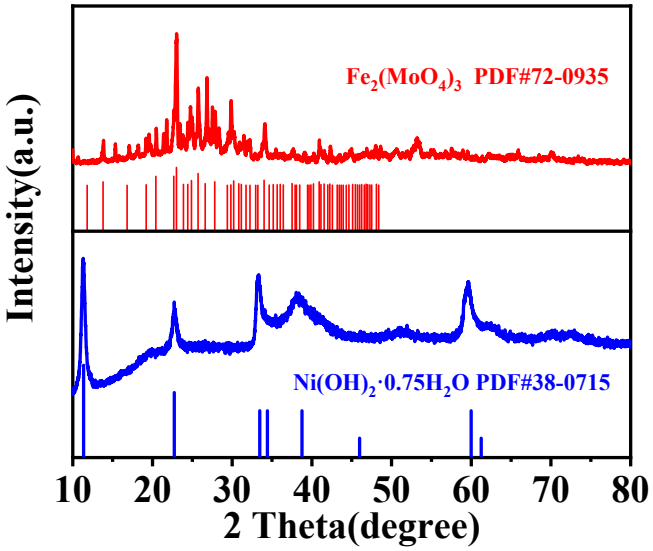

Fig. S1 XRD patterns of $Ni(OH)_2$ and $Fe_2(MoO_4)_3$ powders.

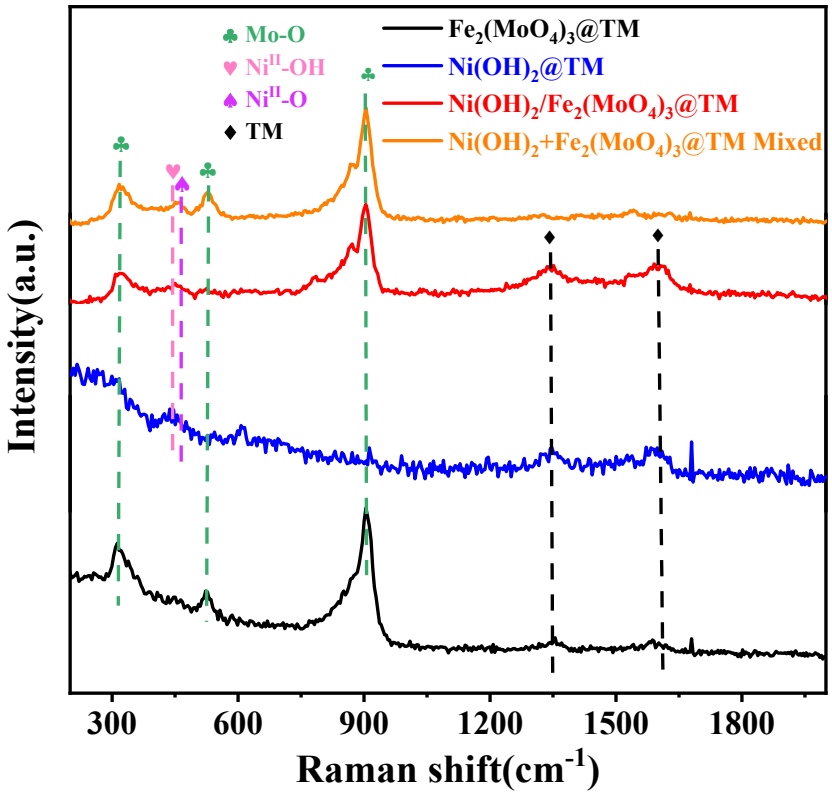

Fig. S2 Raman spectra of $Fe_2(MoO_4)_3$@TM, $Ni(OH)_2$@TM, $Ni(OH)_2/Fe_2(MoO_4)_3$@TM and $Ni(OH)_2$+$Fe_2(MoO_4)_3$ physical mixed powders.

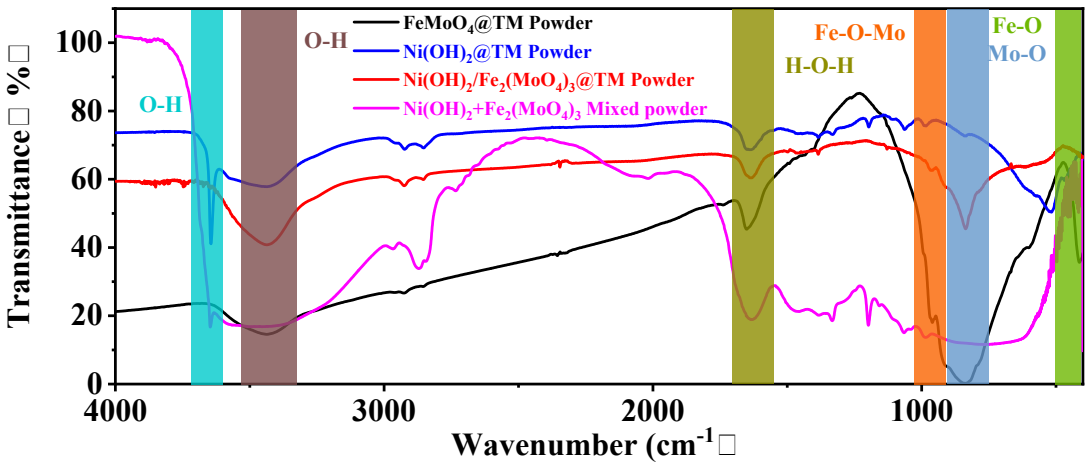

Fig. S3 Infrared spectra of the $Fe_2(MoO_4)_3$@TM, $Ni(OH)_2$@TM, $Ni(OH)_2/Fe_2(MoO_4)_3$@TM and $Ni(OH)_2+Fe_2(MoO_4)_3$ powders.

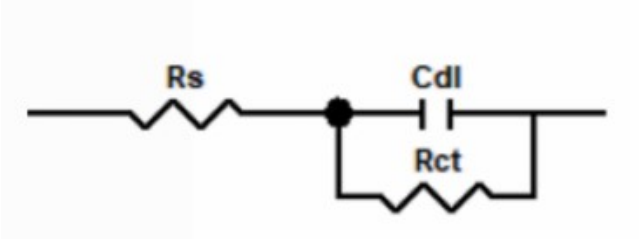

Fig. S4 The electrochemical impedance spectroscopy equivalent circuit diagram.

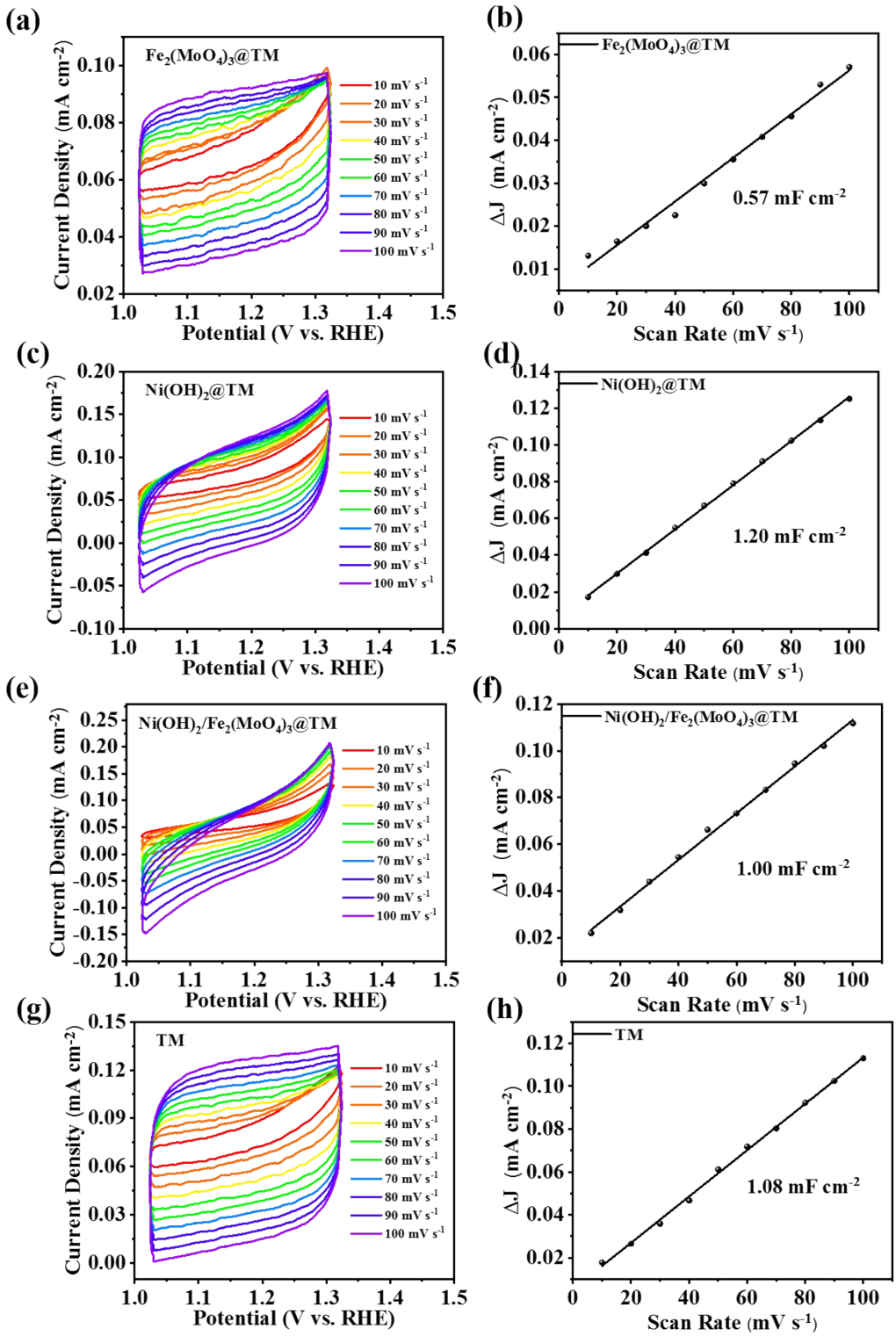

Fig. S5 CV curves of electrodes at different scan rates from 10 to 100 mV s^{-1}.and Electrical-double layer capacitance (a, b) $Fe_2(MoO_4)_3$@TM, (c, d) $Ni(OH)_2$@TM, (e, f) $Ni(OH)_2/Fe_2(MoO_4)_3$@TM, (g, h)TM.

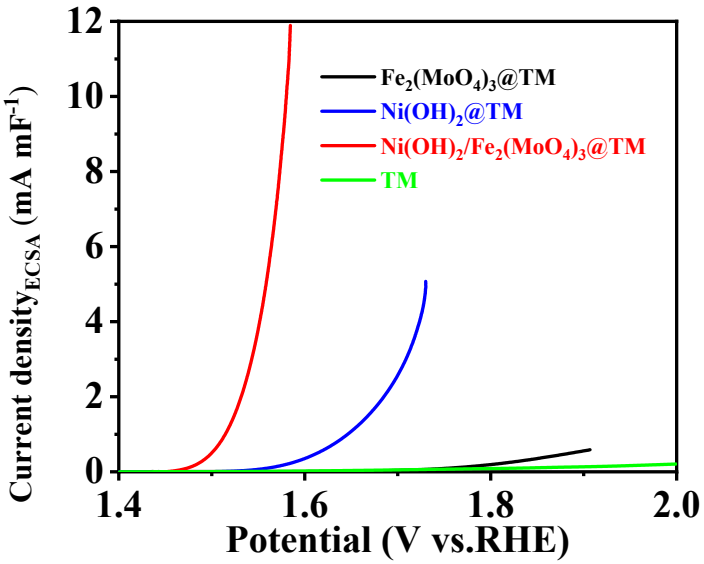

Fig. S6 Normalized LSV curves of $Fe_2(MoO_4)_3$@TM, $Ni(OH)_2$@TM, $Ni(OH)_2/Fe_2(MoO_4)_3$@TM and TM electrodes.

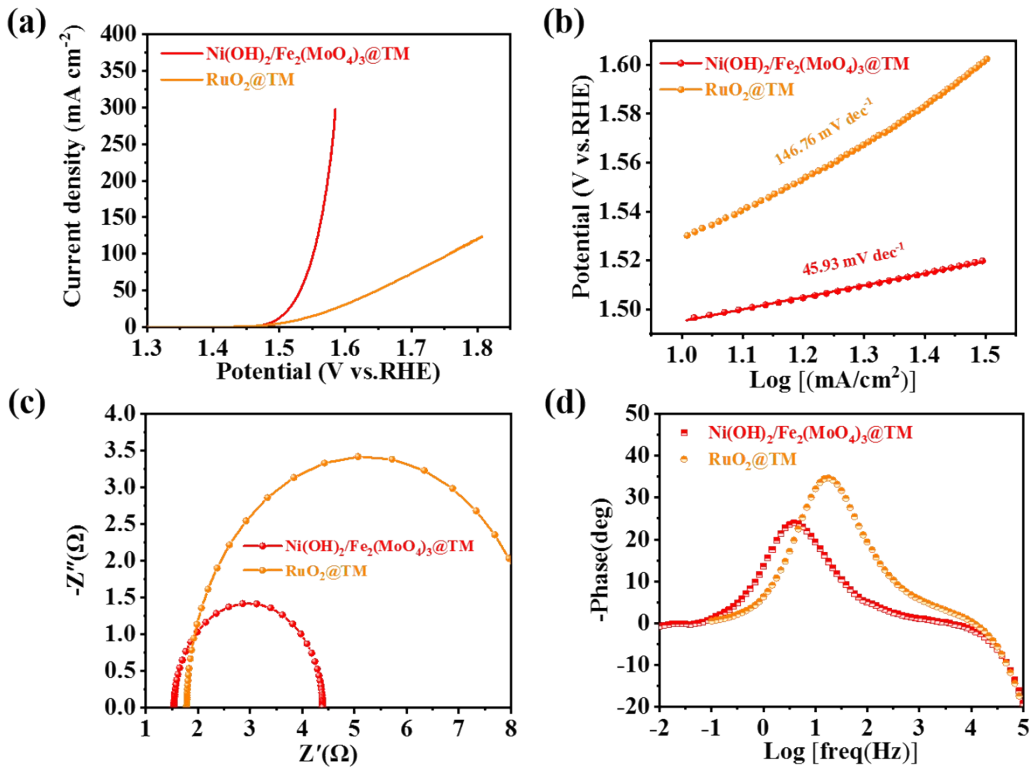

Fig. S7 (a) LSV curve and (b) Tafel slope $Ni(OH)_2/Fe_2(MoO_{4)3}$@TM (c) Nyquist plot and (d) the Bode slope of $Ni(OH)_2/Fe_2(MoO_{4)3}$@TM and RuO_2@TM electrodes.

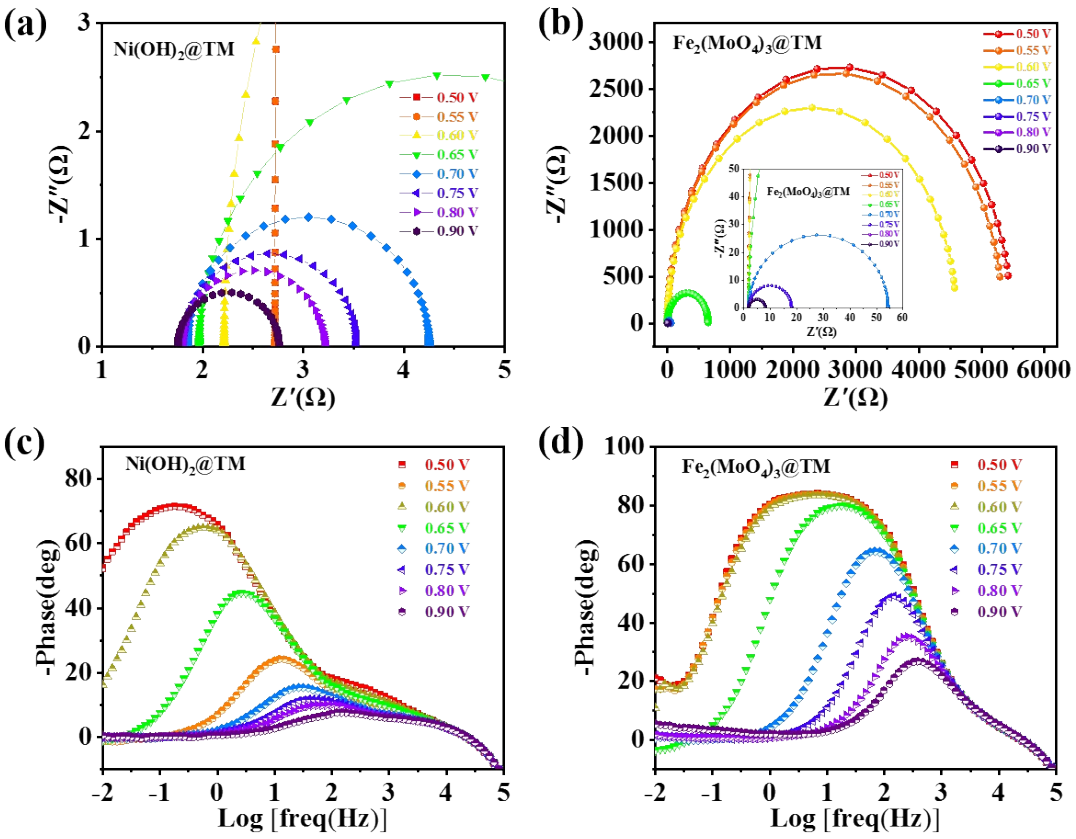

Fig. S8 In-situ (a, b) Nyquist and (c, d) the Bode phase plots of $Fe_2(MoO_4)_3$@TM and $Ni(OH)_2$@TM.

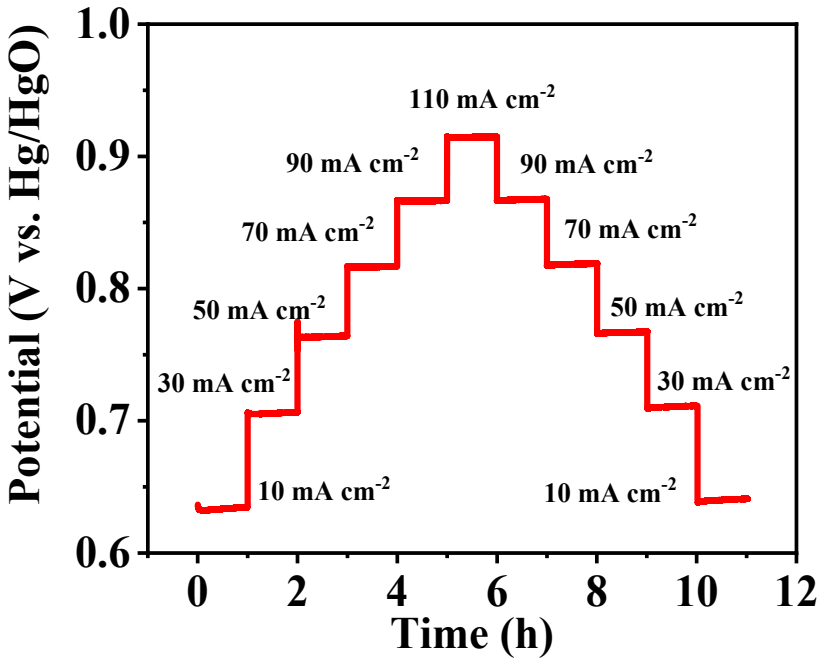

Fig. S9 Multisteps current diagram of $Ni(OH)_2/Fe_2(MoO_4)_3$@TM.

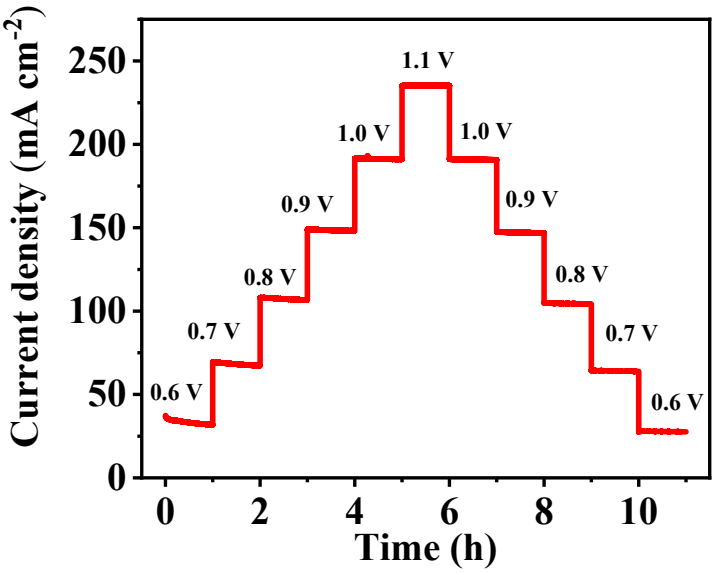

Fig. S10 Multisteps potential diagram of $Ni(OH)_2/Fe_2(MoO_4)_3$@TM.

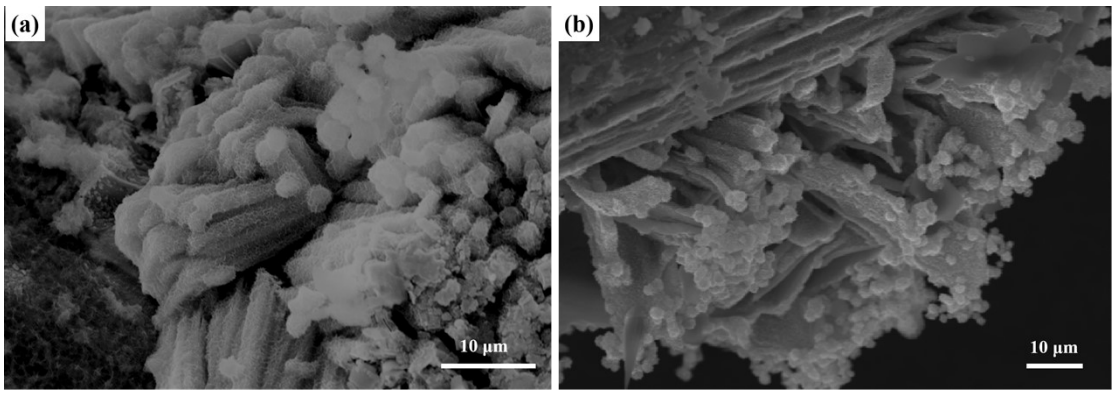

Fig. S11 The SEM morphology of $Ni(OH)_2/Fe_2(MoO_4)_3$@TM (a) before and (b) after OER.

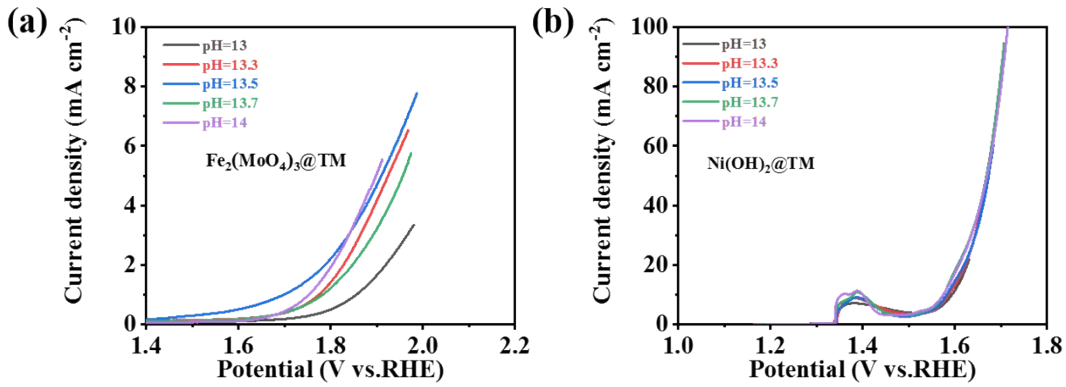

Fig. S12 LSV curves at different pH values of (a) $Fe_2(MoO_4)_3$@TM and (b) $Ni(OH)_2/Fe_2(MoO_4)_3$@TM.

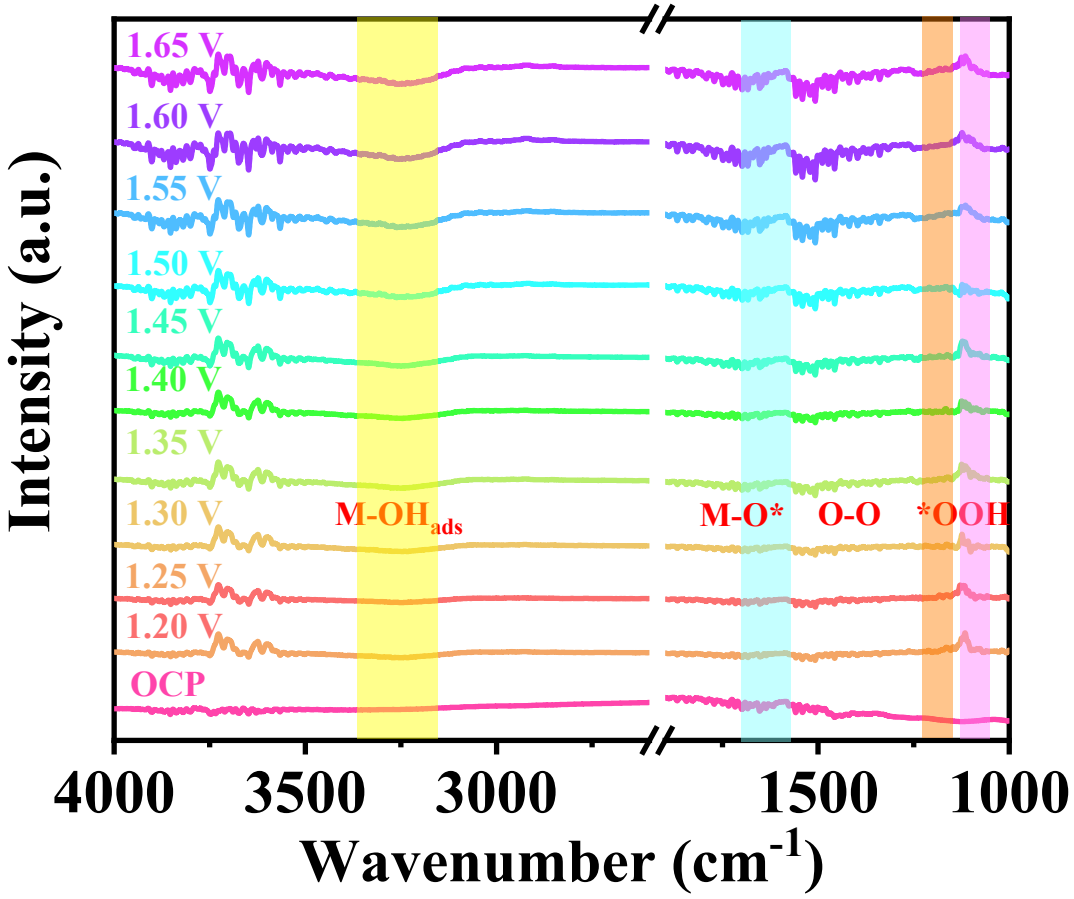

Fig. S13 In-situ ATR-FTIR results of the $Ni(OH)_2$@TM.

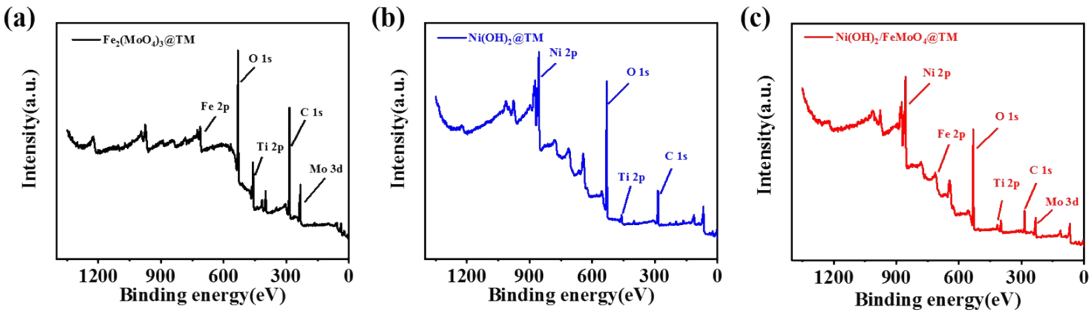

Fig. S14 The XPS spectra of (a) $Fe_2(MoO_4)_3$@TM, (b) $Ni(OH)_2$@TM, (c) $Ni(OH)_2/Fe_2(MoO_4)_3$@TM.

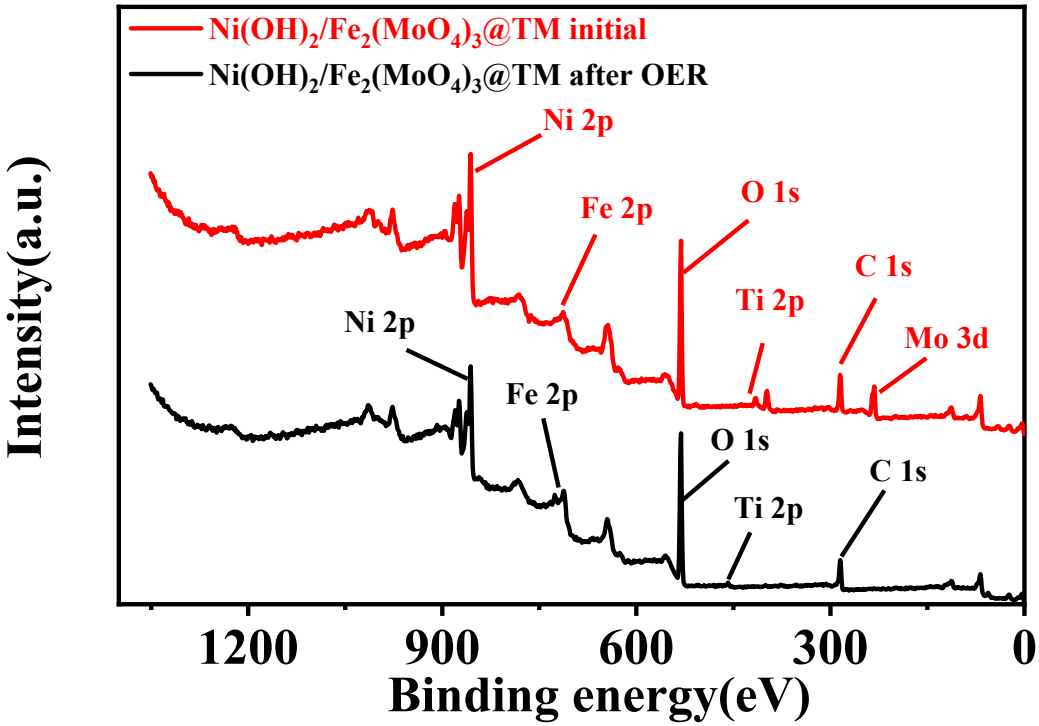

Fig. S15 The initial and after OER XPS spectra of $Ni(OH)_2/Fe_2(MoO_4)_3$@TM.

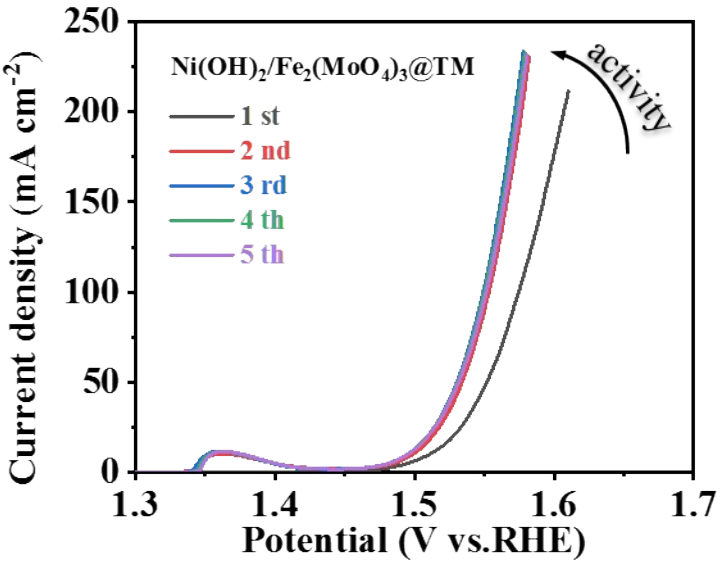

Fig. S16 The activation process of $Ni(OH)_2/Fe_2(MoO_4)_3$@TM under OER condition with 10 mV s^{-1}.

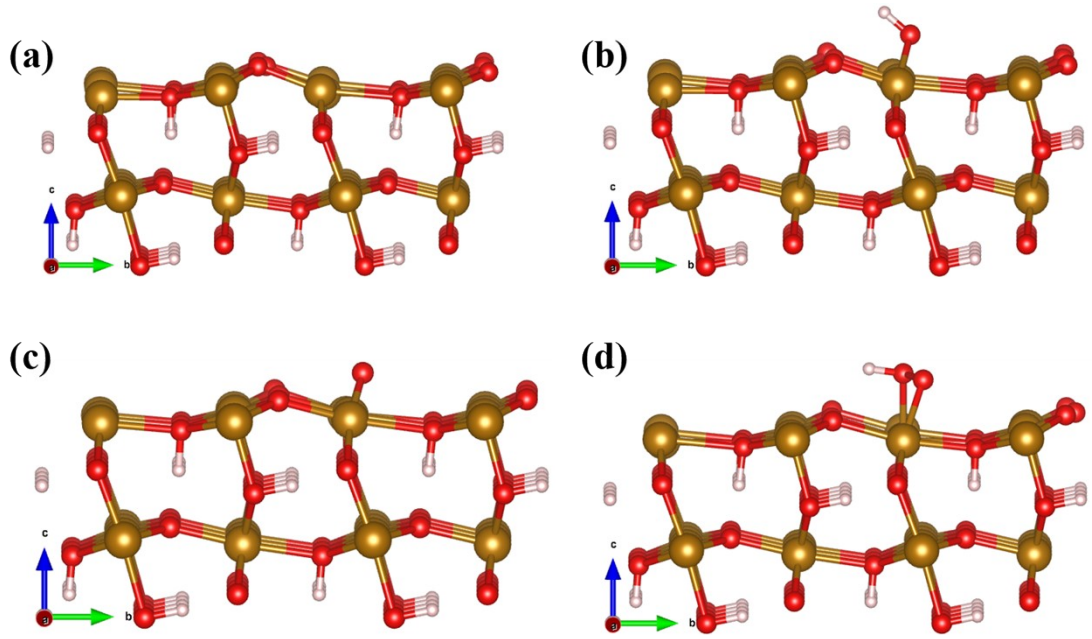

Fig. S17 Optimized configurations of (a) FeOOH and (b) O*,(c) OH*,and (d) OOH* species adsorbed on FeOOH models.

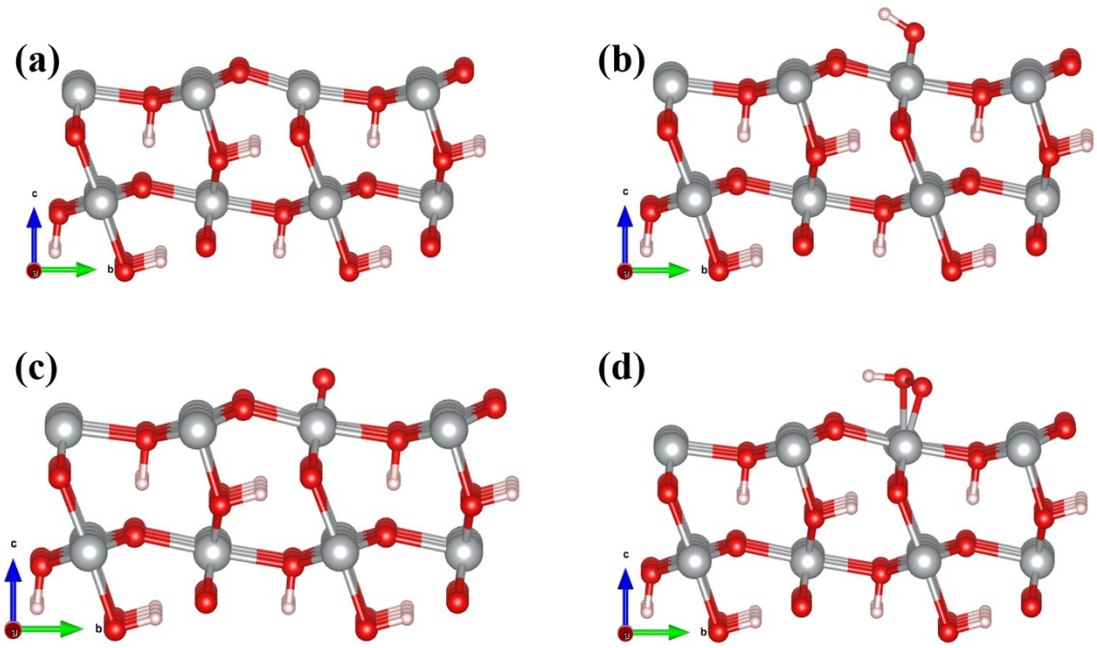

Fig. S18 Optimized configurations of (a) NiOOH and (b) O*,(c) OH*,and (d) OOH* species adsorbed on NiOOH models.

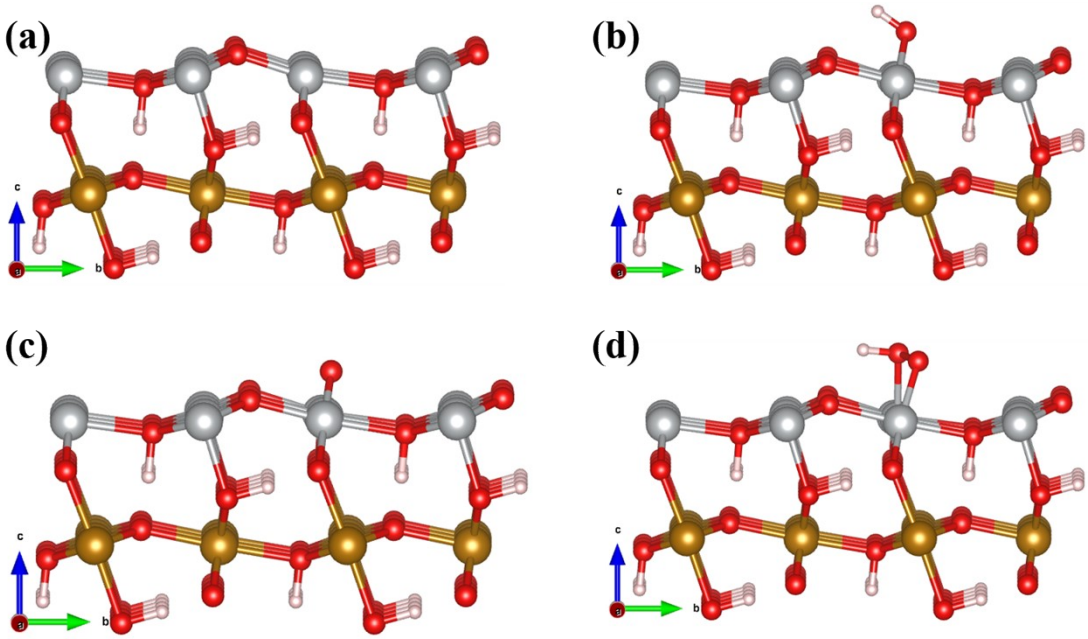

Fig. S19 Optimized configurations of (a) NiOOH(110)/FeOOH and (b) O*,(c) OH*,and (d) OOH* species adsorbed on NiOOH(110)/FeOOH models.

3. Supplementary Tables

Table S1. C_{dl} and ECSA of various catalysts

Catalyst	C_{dl} (mF cm^{-2})	ECSA (cm^2)[a]
$Fe_2(MoO_4)_3$@TM	0.57	14.25
$Ni(OH)_2$@TM	1.20	30.00
$Ni(OH)_2/Fe_2(MoO_4)_3$@TM	1.00	25.00
Titanium Mesh (TM)	1.08	27.00

[a] ECSA of the electrode=C_{dl}/C_s. Cs(the specific capacitance) is generally found to be in the range of 20 μF cm^{-2}-60 μF cm^{-2}. [6, 7] In this work, we used the Cs = 40 μF cm^{-2}.

Table S2. The ICP-MS results of various elements in $Ni(OH)_2/Fe_2(MoO_4)_3$@TM

Sample Weight/g	Elements	Volume/ml	Dilution Coefficient	Instrument Reading/mg L^{-1}	Sample Concentration/mg kg^{-1}
0.0034	Fe	25	1	3.3398	24556.99
0.0034	Ni	25	1	4.8286	35504.71

Table S3. Ni 2p XPS spectra fitting of $Ni(OH)_2/Fe_2(MoO_4)_3$@TM in its initial state and after OER state

Catalyst	Peak	Position(eV)	Area	FWHM (eV)
$Ni(OH)_2/Fe_2(MoO_4)_3$@TM Initial	Satellite	879.84	49560	5.00
	Ni^{3+} $2p_{1/2}$	874.71	23942	3.54
	Ni^{2+} $2p_{1/2}$	872.95	24274	1.83
	Satellite	861.60	67052	4.41
	Ni^{3+} $2p_{3/2}$	856.56	36874	2.11
	Ni^{2+} $2p_{3/2}$	855.25	43000	1.52
$Ni(OH)_2/Fe_2(MoO_4)_3$@TM After OER	Satellite	879.41	43466	5.20
	Ni^{3+} $2p_{1/2}$	874.14	15018	2.20
	Ni^{2+} $2p_{1/2}$	872.81	15964	1.44
	Satellite	861.45	58765	4.60
	Ni^{3+} $2p_{3/2}$	856.28	29155	1.71

	Ni^{2+} $2p_{3/2}$	855.16	31000	1.27

Table S4. Comparison of the OER performance of $Ni(OH)_2/Fe_2(MoO_4)_3$@TM catalyst with other reported OER catalysts

Catalyst	Electrolyte	Substrate	Current density /mA cm^{-2}	Overpotential / mV	Ref
FeOOH/NF	1M KOH	NF	10	390	8
$Ni(OH)_2$/NF	1M KOH	NF	10	350	9
α-$Ni(OH)_2$	1M KOH	GC	10	331	10
Co_3O_4@Ti	1M KOH	TM	20	416	11
$Co(OH)_2$/Ti-2.0	1M KOH	TM	50	316	12
$NiCo_2O_4$/Ti	1M KOH	TM	10	353	13
$IrTiO_{x\text{-}60}ALD_{IrOx}$	1M KOH	TM	10	353	14
RuO_2-IrO_2	0.1M KOH	TM	10	303	15
W-625	1M KOH	stainless steel	10	325	16
Co_3O_4(x)/lsm-TiO_2	1M KOH	TM	10	348	17
Co−S/Ti mesh	1M KOH	TM	10	361	18
$Co_{0.15}$-$Fe_2(MoO_4)_3$	1M KOH	N/A	10	273	19
β-$NiMoO_4$	1M KOH	N/A	10	300	20
$CoMoO_4$-$NiMoO_4$	1M KOH	N/A	10	300	21
NiNiFeMoO/NF	1M KOH	NF	10	255	22
NC/NiMo/$NiMoO_x$/NF	1M KOH	NF	10	284	23
NiMo HNRs/Ti mesh	1M KOH	TM	10	310	24
$Ni_xCo_{3-x}O_4$ NWs/Ti	1M KOH	TM	10	370	25
AP-$CoMoO_4$	1M KOH	NF	10	328	26
$CoMoO_4 \cdot xH_2O$	1M KOH	NF	10	346	27
$CoCrO_x$	1M KOH	carbon paper	100	400	28
LaMN@Co-ZIF	1M KOH	N/A	10	353	29
Co_3O_4@C/GPO	1 M H_2SO_4	N/A	10	360	30
$ZnCo_2O_{4-x}F_x$/CNTs	1M KOH	N/A	10	350	31
Ir-Ni_3N/NF	1M KOH	NF	100	360	32
$Ni(OH)_2/Fe_2(MoO_4)_3$@TM	1M KOH	TM	10 100	265 312	This work

4.Reference

1 G. Kresse, D. Joubert. From ultrasoft pseudopotentials to the projector augmented-wave method, PHYS REV B, 1999, 59, 1758-1775.

2 J.P. Perdew, K. Burke, M. Ernzerhof. Generalized Gradient Approximation Made Simple Phys. Rev. Lett. 77, 3865 (1996), Phys Rev Lett, 1997, 78, 1396-1396.

3 S. Grimme, J. Antony, S. Ehrlich, H. Krieg. A consistent and accurate ab initio parametrization of density functional dispersion correction (DFT-D) for the 94 elements H-Pu, J Chem Phys, 2010, 132, 154104.

4 H.J. Monkhorst, J.D. Pack. Special points for Brillouin-zone integrations, PHYS REV B, 1976, 13, 5188-5192.

5 V. Wang, N. Xu, J.-C. Liu, G. Tang, W.-T. Geng. VASPKIT: A user-friendly interface facilitating high-throughput computing and analysis using VASP code, Comput Phys Commun, 2021, 267, 108033.

6 L. Yang, H. Li, Y. Yu, Y. Wu, L. Zhang. Assembled 3D MOF on 2D Nanosheets for Self-boosting Catalytic Synthesis of N-doped Carbon Nanotube Encapsulated Metallic Co Electrocatalysts for Overall Water Splitting, Applied Catalysis B: Environmental, 2020, 271, 118939.

7 J. Wang, Y. Lian. The self-supporting NiMn-LDHs/rGO/NF composite electrode showing much enhanced electrocatalytic performance for oxygen evolution reaction, Catalysts, 2023, 13, 1012.

8 J. Lee, H. Lee, B. Lim. Chemical transformation of iron alkoxide nanosheets to FeOOH nanoparticles for highly active and stable oxygen evolution electrocatalysts, J Ind Eng Chem, 2018, 58, 100-104.

9 J. Lee, G.-H. Lim, B. Lim. Nanostructuring of metal surfaces by corrosion for efficient water splitting, Chem Phys Lett, 2016, 644, 51-55.

10 M. Gao, W. Sheng, Z. Zhuang, Q. Fang, S. Gu, J. Jiang, Y. Yan. Efficient water oxidation using nanostructured α-nickel-hydroxide as an electrocatalyst, J Am Chem Soc, 2014, 136, 7077-7084.

11 Z. Tao, L. Jiang, X. Jia, H. Xiao, Y. Liang, B. Yang, P. Guo, L. Zhang, H. Yang. In situ growth of Co_3O_4 nanoneedles on titanium mesh for electrocatalytic oxygen evolution, Journal of Materials Science: Materials in Electronics, 2021, 32, 23275-23284.

12 Y. Yan, Y. Chen, M. Shao, X. Chen, Z. Yang, J. Wang, H. Chen, L. Ni, G. Diao, M. Chen. Construction of Ultrathin Cobalt-Based Nanosheet Arrays on Titanium Mesh as Asymmetric Electrodes for Overall Water Splitting, ACS Sustainable Chem Eng, 2023, 11, 2499-2510.

13 W. Bao, L. Xiao, J. Zhang, P. Jiang, X. Zou, C. Yang, X. Hao, T. Ai. Electronic and structural engineering of $NiCo_2O_4$/Ti electrocatalysts for efficient oxygen evolution reaction, Int J Hydrogen Energy, 2021, 46, 10259-10267.

14 M. Frisch, M.H. Raza, M.-Y. Ye, R. Sachse, B. Paul, R. Gunder, N. Pinna, R. Kraehnert. ALD-Coated Mesoporous Iridium-Titanium Mixed Oxides: Maximizing Iridium Utilization for an Outstanding OER Performance, Adv Mater Interfaces, 2022, 9, 2102035.

15 J.E. Park, H. Lee, S.-H. Oh, S.Y. Kang, I. Choi, Y.-H. Cho, Y.-E. Sung. Electrodeposited mesh-type dimensionally stable anode for oxygen evolution reaction in acidic and alkaline media, Chem Eng Sci, 2019, 206, 424-431.

16 L. Magnier, G. Cossard, V. Martin, C. Pascal, V. Roche, E. Sibert, I. Shchedrina, R. Bousquet, V. Parry, M. Chatenet. Fe-Ni-based alloys as highly active and low-cost oxygen evolution reaction catalyst in alkaline media, Nat Mater, 2024, 23, 252-261.
17 M.S. Amer, M.A. Ghanem, P. Arunachalam, A.M. Al-Mayouf, S.M. Hadadi. Bifunctional electrocatalyst of low-symmetry mesoporous titanium dioxide modified with cobalt oxide for oxygen evolution and reduction reactions, Catalysts, 2019, 9, 836.
18 T. Liu, Y. Liang, Q. Liu, X. Sun, Y. He, A.M. Asiri. Electrodeposition of cobalt-sulfide nanosheets film as an efficient electrocatalyst for oxygen evolution reaction, Electrochem Commun, 2015, 60, 92-96.
19 Y. Qian, X. Xu, Y. He, L. Lei, Y. Xia, X. Zhang. A novel monoclinic metal oxide catalyst for oxygen evolution reactions in alkaline media, Inorg Chem Front, 2022, 9, 941-949.
20 S. Ratha, A.K. Samantara, K.K. Singha, A.S. Gangan, B. Chakraborty, B.K. Jena, C.S. Rout. Urea-assisted room temperature stabilized metastable β-$NiMoO_4$: experimental and theoretical insights into its unique bifunctional activity toward oxygen evolution and supercapacitor, ACS applied materials & interfaces, 2017, 9, 9640-9653.
21 Z. Yin, Y. Chen, Y. Zhao, C. Li, C. Zhu, X. Zhang. Hierarchical nanosheet-based $CoMoO_4$-$NiMoO_4$ nanotubes for applications in asymmetric supercapacitors and the oxygen evolution reaction, J Mater Chem A, 2015, 3, 22750-22758.
22 Y.K. Li, G. Zhang, W.T. Lu, F.F. Cao. Amorphous Ni-Fe-Mo suboxides coupled with Ni network as porous nanoplate array on nickel foam: a highly efficient and durable bifunctional electrode for overall water splitting, Adv Sci, 2020, 7, 1902034.
23 J. Hou, Y. Wu, S. Cao, Y. Sun, L. Sun. Active sites intercalated ultrathin carbon sheath on nanowire arrays as integrated core-shell architecture: highly efficient and durable electrocatalysts for overall water splitting, Small, 2017, 13, 1702018.
24 J. Tian, N. Cheng, Q. Liu, X. Sun, Y. He, A.M. Asiri. Self-supported NiMo hollow nanorod array: an efficient 3D bifunctional catalytic electrode for overall water splitting, J Mater Chem A, 2015, 3, 20056-20059.
25 Y. Li, P. Hasin, Y. Wu. $Ni_xCo_{3-x}O_4$ nanowire arrays for electrocatalytic oxygen evolution, Adv Mater, 2010, 17, 1926-1929.
26 H. Xiao, K. Chi, H. Yin, X. Zhou, P. Lei, P. Liu, J. Fang, X. Li, S. Yuan, Z. Zhang, Y. Su, J. Guo, L. Qian. Excess Activity Tuned by Distorted Tetrahedron in $CoMoO_4$ for Oxygen Evolution, Energy environ mater, 2024, 7, e12495.
27 H. Yin, Y. Mo, C. Liu, H. Xiao, Z. Zheng, S. Yuan, J. Guo. Tuning Mo cations dissolution and surface reconstruction of $CoMoO_4$ for efficient oxygen evolution reaction, J Alloys Compd, 2024, 985, 173963.
28 S. Li, T. Liu, W. Zhang, M. Wang, H. Zhang, C. Qin, L. Zhang, Y. Chen, S. Jiang, D. Liu, X. Liu, H. Wang, Q. Luo, T. Ding, T. Yao. Highly efficient anion exchange membrane water electrolyzers via chromium-doped amorphous electrocatalysts, Nat Commun, 2024, 15, 3416.
29 L. Chong, G. Gao, J. Wen, H. Li, H. Xu, Z. Green, J.D. Sugar, A.J. Kropf, W. Xu, X.-M. Lin, H. Xu, L.-W. Wang, D.-J. Liu. La- and Mn-doped cobalt spinel oxygen evolution catalyst for proton exchange membrane electrolysis, Science, 2023, 380, 609-616.
30 J. Yu, F.A. Garcés-Pineda, J. González-Cobos, M. Peña-Díaz, C. Rogero, S. Giménez, M.C. Spadaro, J. Arbiol, S. Barja, J.R. Galán-Mascarós. Sustainable oxygen evolution electrocatalysis in aqueous 1 M H2SO4 with earth abundant nanostructured Co_3O_4, Nat Commun, 2022, 13, 4341.

31 K. Xiao, Y. Wang, P. Wu, L. Hou, Z.-Q. Liu. Activating Lattice Oxygen in Spinel $ZnCo_2O_4$ through Filling Oxygen Vacancies with Fluorine for Electrocatalytic Oxygen Evolution, Angew Chem Int Ed, 2023, 62, e202301408.
32 Y. Chen, J. Meng, M. Xu, L. Qiao, D. Liu, Y. Kong, X. Hu, Q. Liu, M. Chen, S. Lyu, R. Tong, H. Pan. Adaptive Active Site Turning for Superior OER and UOR on Ir-Ni_3N Catalyst, Adv Funct Mater, 2024, 35, 2413474.